
DANBO: Disentangled Articulated Neural Body Representations via Graph Neural Networks

Shih-Yang Su¹ Timur Bagautdinov² Helge Rhodin¹

¹University of British Columbia ²Reality Labs Research



Figure 1: DANBO enables learning volumetric body models from scratch, only requiring a single video as input, yet enable driving by unseen poses (inset) that are out of the training distribution, showing better robustness than existing surface-free approaches. **Real faces are blurred for anonymity.**

Abstract

Deep learning greatly improved the realism of animatable human models by learning geometry and appearance from collections of 3D scans, template meshes, and multi-view imagery. High-resolution models enable photo-realistic avatars but at the cost of requiring studio settings not available to end users. Our goal is to create avatars directly from raw images without relying on expensive studio setups and surface tracking. While a few such approaches exist, those have limited generalization capabilities and are prone to learning spurious (chance) correlations between irrelevant body parts, resulting in implausible deformations and missing body parts on unseen poses. We introduce a three-stage method that induces two inductive biases to better disentangle pose-dependent deformation. First, we model correlations of body parts explicitly with a graph neural network. Second, to further reduce the effect of chance correlations, we introduce localized per-bone features that use a factorized volumetric representation and a new aggregation function. We demonstrate that our model produces realistic body shapes under challenging unseen poses and shows high-quality image synthesis. Our proposed representation strikes a better trade-off between model capacity, expressiveness, and robustness than competing methods. Project website: <https://lemonatsu.github.io/danbo>.

1 Introduction

Animating real-life objects in the digital world is a long-pursued goal in computer vision and graphics, and recent advances already enable 3D free-viewpoint video, animation, and human perfor-

mance retargeting Gao et al. [2021], Peng et al. [2021b], Xian et al. [2021]. Nevertheless, animating high-definition virtual avatars with user-specific appearance and dynamic motion still remains a challenge: human body and clothing deformation are inherently complex, unique, and modeling their intricate effects require dedicated approaches. Recent solutions achieve astonishing results Chen et al. [2021], Liu et al. [2021], Saito et al. [2021], Tiwari et al. [2020, 2021] when grounding on 3D data capture in designated studio settings, e.g., with multi-camera capture systems and controlled illumination—inaccessible to the general public for building personalized models.

Less restrictive are methods relying on parametric body models Loper et al. [2015] that learn plausible body shape, pose, and deformation from a collection of 3D scans. These methods can thereby adapt to a wide range of body shapes Balan et al. [2007], Choutas et al. [2020], Osman et al. [2020], in particular when using neural approaches to model details as a dynamic corrective Bhatnagar et al. [2020], Burov et al. [2021], Corona et al. [2021]. Even though subject-specific details such as clothing can be learned, it remains difficult to generalize to shapes vastly different from the original scans. Moreover, the most widely used body models have restrictive commercial licenses Loper et al. [2015] and 3D scan datasets to train these afresh are expensive.

Our goal is to learn a high-quality model with subject-specific details directly from images. Recent approaches in this class Noguchi et al. [2021], Su et al. [2021] use a neural radiance field (NeRF) that is attached to a human skeleton initialized with an off-the-shelf 3D human pose estimator. Similar to the original NeRF, the shape and appearance are modeled implicitly with a neural network that takes as input a query location and outputs density and radiance, and is only supervised with images through differentiable volume rendering. However, unlike the original that models static scenes, articulated NeRFs model time-varying body shape deformations by conditioning on per-frame body pose and representing each frame with the same underlying body model albeit in a different state. This results in an animatable full-body model that is trained directly from videos and can then be driven with novel skeleton poses.

Not using an explicit surface poses a major difficulty as surface-based solutions exploit surface points to anchor neural features locally as vertex attributes Peng et al. [2021b], and leverage skinning weights to associate points on or close to the surface to nearby body parts Liu et al. [2021], Peng et al. [2021a]. In absence of such constraints, A-NeRF Su et al. [2021] uses an overparametrization by encoding 3D position relative to all body parts. Thereby dependencies between a point and body parts are learned implicitly. By contrast, NARF Noguchi et al. [2021] explicitly predicts probabilities for the association of 3D points to body parts, similar to NASA Deng et al. [2019]. However, this probability predictor is conditioned on the entire skeleton pose and is itself prone to poor generalization. Therefore, both approaches rely on large training datasets and generalization to unseen poses is limited—in particular because unrelated body parts remain weakly entangled.

In this paper, we introduce *Disentangled Articulated Neural BOdy* (DANBO), a surface-free approach that explicitly disentangles independent body parts for learning a generalizable personalized human model from unlabelled videos. It extends the established articulated NeRF-based body modeling with two additional stages, a body part-specific volumetric encoding that exploits human skeleton structure as a prior using Graph Neural Networks (GNN) Kipf and Welling [2017], and a new aggregation module. Both designs are tailored for learning from few examples and optimized to be parameter efficient. Our main contributions are the following:

- A surface-free human body model with better texture detail and improved generalization when animated.
- GNN-based encoding that disentangles features from different body parts and relies on factorized per-bone volumes for efficiency.
- A part-based feature aggregation strategy that improves on and is informed by a detailed evaluation of existing aggregation functions.

We demonstrate that our proposed DANBO results in a robust neural body model, with quality comparable to surface-based approaches.

2 Related Work

We start our review with general-purpose neural fields and then turn to human body modeling with a focus on animatable neural representations.

Neural fields. Neural fields Mildenhall et al. [2020], Park et al. [2019], Sitzmann et al. [2020] have attracted recent attention due to their ability to capture astonishing levels of detail. Instead of relying on explicit geometry representations such as triangle meshes or voxel grids, these methods represent the scene implicitly - as a continuous function - that maps every point in the 3D space to quantities of interest such as radiance, density, or signed distance. This approach was popularized with Neural Radiance Fields (NeRF) Mildenhall et al. [2020] demonstrating impressive results on reconstructing static 3D scene presentation directly from calibrated multi-view images. Various subsequent works focused on improving performance on static scenes in terms of generalization Yu et al. [2021b], level of detail Barron et al. [2021], Park et al. [2021], camera self-calibration Lin et al. [2021], Yen-Chen et al. [2020], and resource efficiency Lindell et al. [2021], Yu et al. [2021a]. Most relevant are deformable models that capture non-static scenes with deformation fields Gafni et al. [2021], Gao et al. [2021], Pumarola et al. [2020], Tretschk et al. [2021], Xian et al. [2021]. However, general deformation fields are unsuitable for animation and no one demonstrated that they can generalize to strongly articulated motion in monocular video.

Template-based body models. The highest level of detail can be attained with specialized performance capture systems, e.g., with dozens of cameras or a laser scanner Guo et al. [2019]. The resulting template mesh can then be textured and deformed for capturing high-quality human performances, even from a single video Zhou et al. [2018]. Neural approaches further enable learning pose-dependent appearance and geometries Bagautdinov et al. [2021], predict vertex displacements Habermann et al. [2021] or local primitive volumes Lombardi et al. [2021] for creating fine-grained local geometry and appearance including cloth wrinkles and freckles. The most recent ones use neural fields to learn implicit body models with the mesh providing strong supervision signals Alldieck et al. [2021], Chen et al. [2021], Saito et al. [2021], Wang et al. [2021], Xu et al. [2021]. However, template creation is limited to expensive controlled studio environments, often entails manual cleaning, and high-quality ground truth annotations.

Parametric Human Body Models learn common shape and pose properties from a large corpus of 3D scans Balan et al. [2007], Choutas et al. [2020], Loper et al. [2015], Osman et al. [2020]. For classical approaches the result are factorized parameters for controlling pose, shape Choutas et al. [2020], Loper et al. [2015], Osman et al. [2020], Xu et al. [2020] and even clothing Tiwari et al. [2020] that can fit to a new subject. Most prevalent is the SMPL Choutas et al. [2020], Loper et al. [2015] mesh model with a linear shape space and pose-dependent deformation. However, most existing models have restrictive commercial licenses and modeling person-specific details from images requires additional reconstruction steps.

Personalized Body Models. Learning personalized body models given only videos of a single actor is particularly challenging. Most existing approaches start from estimating a parametric surface model such as SMPL and extend it to learn specifics. For instance, one can anchor neural features spatially by associating each SMPL vertex with a learnable latent feature, and then either diffuse vertex features to the 3D space Kwon et al. [2021], Peng et al. [2021b] or project the 3D query point to the SMPL surface for feature retrieval. Incorrect shape estimates and missing details can then be corrected by a subsequent neural rendering step. As texturing improves classical approaches, neural texture mapping provides additional rendering quality Liu et al. [2021]. Another line of work makes use of SMPL blend skinning weights as initialization for learning deformation fields Peng et al. [2021a]. The deformation field maps 3D points from 3D world space to canonical space, which enables learning a canonical neural body field that predicts the radiance and density for rendering as for the classical NeRF on static scenes. While the skinning weights in SMPL provide an initialization, Peng et al. [2021a] showed that fine-tuning the deformation fields via self-supervision helps rendering unseen poses. However, relying on body models imposes the previously discussed limitations.

There are few methods that target learning neural body fields from images without relying on an explicit surface model. Closest to our method are NARF Noguchi et al. [2021] and A-NeRF Su et al. [2021], that learn articulated body models directly from image sequences, leveraging 3D body pose estimates produced by off-the-shelf approaches Kolotouros et al. [2019], Kocabas et al. [2020]. These methods encode 3D query points with respect to each bone on the posed skeleton, and either explicitly predict blending weights Noguchi et al. [2021] to select the parts of influence or rely on a neural network to learn the assignment implicitly by feeding it a large stack of all relative posi-

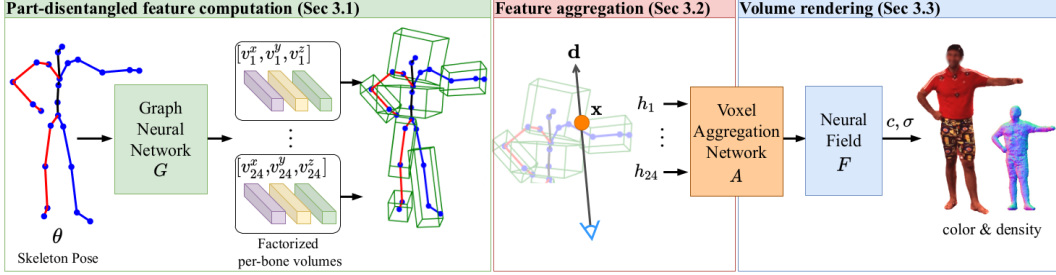


Figure 2: Overview. The final image is generated via volume rendering by sampling points \mathbf{x} along the ray \mathbf{d} as in the original NeRF. Different is the conditioning on pose. First, pose features are encoded locally to every bone of a skeleton with a graph neural network using factorized volumes to increase efficiency (green boxes). Second, these disentangled features are queried and aggregated with learned weights (red module). Finally, the body shape and appearance are predicted via density and radiance fields σ and c (blue module).

tions Su et al. [2021]. However, lacking a prior for part assignments leads to spurious dependencies between irrelevant body parts when the training poses are scarce and have low diversity Bagautdinov et al. [2021], Saito et al. [2021]. Our approach follows the same surface-free setting but improves upon these by introducing body part disentangled representations and a new aggregation function that achieves better rendering quality and improved generalization on novel body poses.

3 Method

Our goal is to learn an animatable avatar from a collections of N images $[\mathbf{I}_k]_{k=1}^N$ and the corresponding body pose in terms of skeleton joint angles $[\theta_k]_{k=1}^N$ that can stem from an off-the-shelf estimator Kolotouros et al. [2019], Kocabas et al. [2020], without using laser scans or surface tracking. We represent the human body as a neural field that moves with the input body pose. The neural field maps each 3D location to color and density to generate a free-viewpoint synthetic image via volume rendering. See Figure 2 for an overview. Our approach consists of three stages that are trained end-to-end. The first stage predicts a localized volumetric representation for each body part with a Graph Neural Network (GNN). GNN has a limited receptive field and encodes only locally relevant pose information—which naturally leads to better disentangling between body parts in the absence of surface priors. This stage is independent of the query locations and is thus executed only once per frame. Additional performance is gained by using a factorized volume and encouraging the volume bounds to be compact. The second stage retrieves a feature code for each query point by sampling volume features for all body parts that enclose the point and then aggregating the relevant ones using a separate network that predicts blend weights. Finally, the third stage maps the resulting per-query feature code to the density and radiance at that location, followed by the volume rendering as in the original NeRF.

3.1 Stage I: Part-disentangled Feature Computation

Given a pose $\theta = [\omega_1, \omega_2, \dots, \omega_{24}]$, where $\omega_i \in \mathbb{R}^6$ Zhou et al. [2019] defines the rotation of the bone $i = 1, 2, \dots, 24$, we represent the body part attached to each bone i with a coarse volume V (green boxes in Fig. 2), predicted by a neural network G ,

$$[V_1, V_2, \dots, V_{24}] = G(\theta). \quad (1)$$

We design G as a GNN operating on the skeleton graph with nodes initialized to the corresponding joint angles in θ . In practice, we use two graph convolutional layers followed by per-node 2-layer MLPs. Because the human skeleton is irregular, we learn individual MLP weights for every node. See the supplemental for additional details on the graph network.

Factorized volume. A straight-forward way to represent a volume is via a dense voxel grid, which has cubic complexity with respect to its resolution. Instead, we propose to factorize each volume $V_i = (v_i^x, v_i^y, v_i^z)$ as one vector $v_i \in \mathbf{R}^{H \times M}$ for each 3D axis, where H is the voxel feature channel,

and is M the volume resolution. This is similar to Peng et al. [2020] doing a factorization into 2D planes.

Figure 3 shows how to retrieve a feature for a given 3D point $\hat{\mathbf{x}}_i$ from the volume by projecting to each axis and interpolating,

$$h_i^x = v_i^x [s_i^x \hat{\mathbf{x}}_i(x)] \in \mathbf{R}^H, \quad (2)$$

where s_i^x is a learnable scaling factor to control the volume size along the x-axis, and $v_i^x[\cdot]$ returns the interpolated feature when the projected and scaled coordinate falls in $[-1, 1]$, and $\mathbf{0}$ otherwise. The extraction for y and z axes follows the same procedure.

The GNN attaches one factorized volume to every bone i and is computed only once for every pose. In Section 4.3, we show that the factorized volumes compare favorably against full 3D volumes on short video sequences with sparse or single views, while having 2x lower parameter counts.

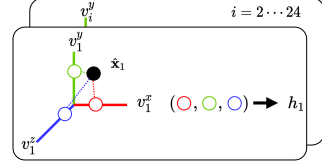


Figure 3: We retrieve the voxel feature by projecting $\hat{\mathbf{x}}$ to the three axes and linearly interpolating the feature neighboring the projected location.

3.2 Stage II: Global Feature Aggregation

Given a query location $\mathbf{x} \in \mathbf{R}^3$ in global coordinates, the corresponding voxel feature can be retrieved by first mapping the 3D points to the bone-relative space of i via the world-to-bone coordinates transformation $T(\omega_i)$,

$$\begin{bmatrix} \hat{\mathbf{x}}_i \\ 1 \end{bmatrix} = T(\omega_i) \begin{bmatrix} \mathbf{x} \\ 1 \end{bmatrix}, \quad (3)$$

and then retrieving the factorized features with equation Eq. 2. However, multiple volumes can overlap.

Windowed bounds. To facilitate learning volume dimensions s_x that adapt to the body shape and to mitigate seam artifacts, we apply a window function

$$w_i = \exp(-\alpha(\hat{\mathbf{x}}_i(x)^\beta + \hat{\mathbf{x}}_i(y)^\beta + \hat{\mathbf{x}}_i(z)^\beta)) \quad (4)$$

that attenuates the feature value $h_i = w_i [h_i^x, h_i^y, h_i^z]$ for $\hat{\mathbf{x}}_i$ towards the boundary of the volume, with $\alpha = 2$ and $\beta = 6$ similar to Lombardi et al. [2021]. Still, multiple volumes will overlap near joints and when body parts are in contact. Moreover, the overlap changes with varying skeleton pose, demanding for an explicit aggregation step.

Voxel Aggregation Network. Since an \mathbf{x} that is close to the body falls into multiple volumes, we employ a voxel aggregation network A to decide which per-bone voxel features to pass on to the downstream neural field for rendering. We explore several strategies, and conduct ablation studies on each of the options. Our aggregation network A consists of a graph layer followed by per-node 2-layer MLPs with a small network width (32 per layer). We predict the weight p_i for the feature retrieved from bone i and compute the aggregated features via

$$p_i = A_i(h_i), \text{ and aggregated feature } \hat{h} = \sum_{i=1}^{24} p_i h_i. \quad (5)$$

Below, we discuss the three strategies for computing the aggregation weights.

Concatenate. Simply concatenating all features lets the network disentangle individual factors, which is prone to overfitting as no domain knowledge is used.

Softmax-OOB. Instead of simply using Softmax to obtain sparse and normalized weights as in Deng et al. [2019], Noguchi et al. [2021], we can make use of our volume representation to remove the influence of irrelevant bones

$$p_i = \frac{(1 - o_i) \exp(a_i)}{\sum_{j=1}^{24} (1 - o_j) \exp(a_j)}, \quad (6)$$

where o_i is the out-of-bound (OOB) indicator which equals to 1 when $\hat{\mathbf{x}}_i$ is not inside of V_i . The potential caveat is that \hat{h} is still susceptible to features from irrelevant volumes. For instance, Figure 4 shows that Softmax-OOB produces artifacts when the hand gets close to the chest.

Soft-softmax Due to the design of A , the output logit a_i of bone i is only dependent on itself. We can leverage this design to obtain the weight for each V_i independently and normalize their range to $[0, 1]$ with a sigmoid function,

$$p_i = (1 - o_i) \cdot S(a_i), \text{ where } S = \frac{1}{1 + \exp(-a_i)}. \quad (7)$$

To nevertheless ensure that aggregated features are in the same range irrespectively of the number of contributors, we introduce a *soft-softmax* constraint

$$L_s = \sum_{\mathbf{x}} \left(\sum_{i=1}^{24} (1 - o_i) p_i - l_{\mathbf{x}} \right)^2, \quad (8)$$

that acts as a soft normalization factor opposed to the hard normalization in softmax. By setting $l_{\mathbf{x}} = 1$ if $T_{\mathbf{x}} \cdot \sigma_{\mathbf{x}} > 0$ and 0 otherwise, the loss enforces the sum of weights of the activated bones to be close to 1 when the downstream neural field has positive density prediction σ (e.g., when \mathbf{x} belong to the human body), and 0 otherwise. The results is a compromise between an unweighted sum and softmax that attained the best generalization in our experiments. A representative improvement on softmax is shown in Figure 4-right.



Figure 4: The influence of aggregation strategies.

3.3 Stage III: Neural Field and Volume Rendering

The aggregated features \hat{h} contain the coarse, pose-dependent body features at location \mathbf{x} . To obtain high-quality human body, we learn a neural field F to predict the refined radiance c and density σ for \mathbf{x}

$$(c, \sigma) = F(\hat{h}, \mathbf{d}), \quad (9)$$

where $\mathbf{d} \in \mathbf{R}^2$ is the view direction. We can then render the image of the human subject by volume rendering as in the original NeRF Mildenhall et al. [2020],

$$\hat{\mathbf{I}}(u, v; \theta) = \sum_{q=1}^Q T_q (1 - \exp(-\sigma_q \delta_q)) c_q, \quad T_q = \exp\left(-\sum_{j=1}^{q-1} \sigma_j \delta_j\right). \quad (10)$$

Given the pose θ , the predicted image color at the 2D pixel location $\hat{\mathbf{I}}(u, v; \theta)$ is computed by integrating the predicted color c_q of the Q 3D samples along \mathbf{d} . δ_q is the distance between neighboring samples, and T_q represents the accumulated transmittance at sample q .

3.4 Training

Our model is directly supervised with ground truth images via photometric loss

$$L_p = \sum_{(u,v) \in \mathbf{I}} |\hat{\mathbf{I}}(u, v; \theta) - \mathbf{I}(u, v; \theta)|. \quad (11)$$

We use L1 loss to avoid overfitting to appearance changes that cannot be explained by pose deformation alone. To prevent the per-bone volumes from growing too large and taking over other volumes, we employ a volume loss as in Lombardi et al. [2021]

$$L_v = \sum_{i=1}^{24} (s^x \cdot s^y \cdot s^z). \quad (12)$$

For Soft-softmax in Section 3.2, we further regularize the output weights via the self-supervised loss L_s .

To summarize, the training objective of our approach is

$$L = L_p + \lambda_v L_v + \lambda_s L_s. \quad (13)$$

We set both λ_v and λ_s to 0.001 for all experiments.

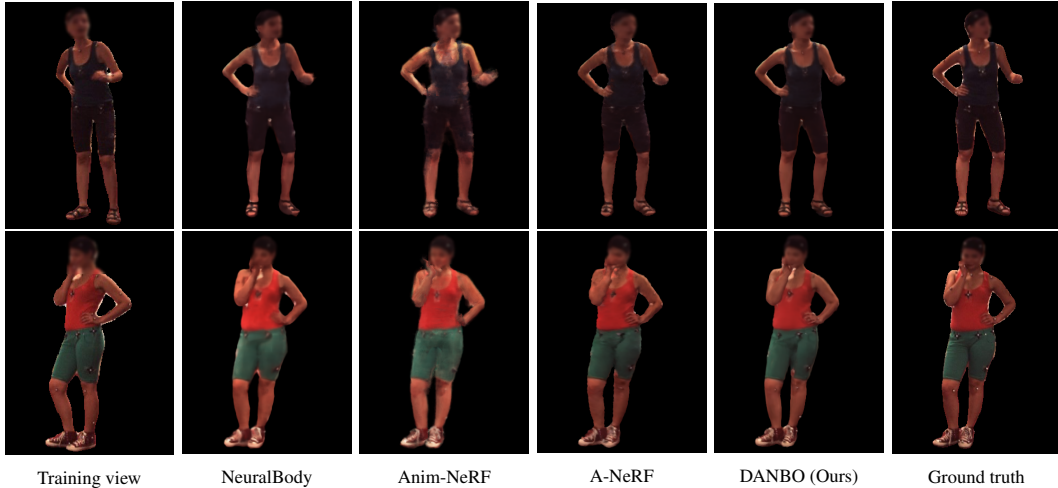


Figure 5: **Novel-view synthesis results on Human3.6M Ionescu et al. [2014]**. DANBO renders more complete limbs and clearer facial features than the baselines.

3.5 Implementation Details

We train our model for 200k iterations, with the same learning rate decay schedule as in Mildenhall et al. [2020]. We use a hyperparameter setting similar to that in A-NeRF Su et al. [2021], with several exceptions. For each training batch, we sample 3072 rays from 16 images with 96 uniform samples and 48 importance samples along each ray. This results in the same number of network evaluations as A-NeRF. Additionally, unlike the original NeRF, we learn a single neural field instead of two separate coarse and fine networks. We use $M = 16$ and $H = 5$ for the factorized volumes in all experiments unless stated otherwise. Training takes around 20 hours on 2 NVidia V100 GPUs. Following prior work, we also optimize a 128-dim latent code for each frame to model the appearance changes that cannot be explained by the skeleton pose alone Martin-Brualla et al. [2021], Peng et al. [2021b], Su et al. [2021]. See the supplemental for more details.

4 Experiments

In the following, we evaluate the improvements upon the most recent surface-free neural body model A-NeRF Su et al. [2021], and compare against recent model-based solutions NeuralBody Peng et al. [2021b] and Anim-NeRF Peng et al. [2021a] and include NT Thies et al. [2019] that synthesizes texture for 3D meshes, and NHR Wu et al. [2020] that extracts 3D point cloud features for rendering human body as baselines. An ablation study further quantifies the improvement of using the proposed aggregation function, local GNN features, and factorized volumes over simpler and more complex Lombardi et al. [2021] alternatives, including the effects on model capacity. The supplemental materials provide additional qualitative results, including videos of retargeting applications.

Metrics and protocols. Our goal is to analyze the quality of synthesizing novel views and separately the rendering of previously unseen poses. Both are measured by the PSNR and SSIM Wang et al. [2004] scores computed over frames withheld from training, following two established protocols:

- Novel view synthesis is evaluated on multi-view datasets by learning the body model from a subset of cameras with the remaining ones used as the test set, i.e. rendering the same pose from the unseen view.
- Novel pose synthesis quality is measured by training on the first part of a video and testing on the latter frames, given their corresponding 3D pose as input. This assumes that only the pose changes as the person moves and that illumination stays constant.

As the background image is not our focus, we report scores on tight bounding boxes either provided by the dataset or computed from the 3D poses.

Table 1: **Novel-view synthesis comparisons on Human3.6M Ionescu et al. [2014].** The disentangled feature enables DANBO to achieve better performance for novel view synthesis.

	NHRWu et al. [2020]		NT Thies et al. [2019]		NeuralBody Peng et al. [2021b]		Anim-NeRF Peng et al. [2021a]		A-NeRF Su et al. [2021]		DANBO (Ours)	
	PSNR \uparrow	SSIM \uparrow	PSNR \uparrow	SSIM \uparrow	PSNR \uparrow	SSIM \uparrow	PSNR \uparrow	SSIM \uparrow	PSNR \uparrow	SSIM \uparrow	PSNR \uparrow	SSIM \uparrow
S1	21.79	0.892	22.04	0.893	22.88	0.897	22.74	0.896	23.93	0.912	23.95	0.916
S5	21.37	0.892	20.91	0.887	24.61	0.917	23.40	0.895	24.67	0.919	24.86	0.924
S6	21.05	0.854	21.10	0.855	22.83	0.888	22.85	0.871	23.78	0.887	24.54	0.903
S7	21.11	0.890	21.59	0.891	23.17	0.915	21.97	0.891	24.40	0.917	24.45	0.920
S8	19.80	0.889	17.69	0.871	21.72	0.894	22.82	0.900	22.70	0.907	23.36	0.917
S9	23.77	0.898	23.80	0.899	24.29	0.911	24.86	0.911	25.58	0.916	26.15	0.925
S11	22.65	0.891	22.73	0.892	23.70	0.896	24.76	0.907	24.38	0.905	25.58	0.917
Avg	21.65	0.887	21.41	0.884	23.31	0.903	23.34	0.896	24.21	0.909	24.70	0.917

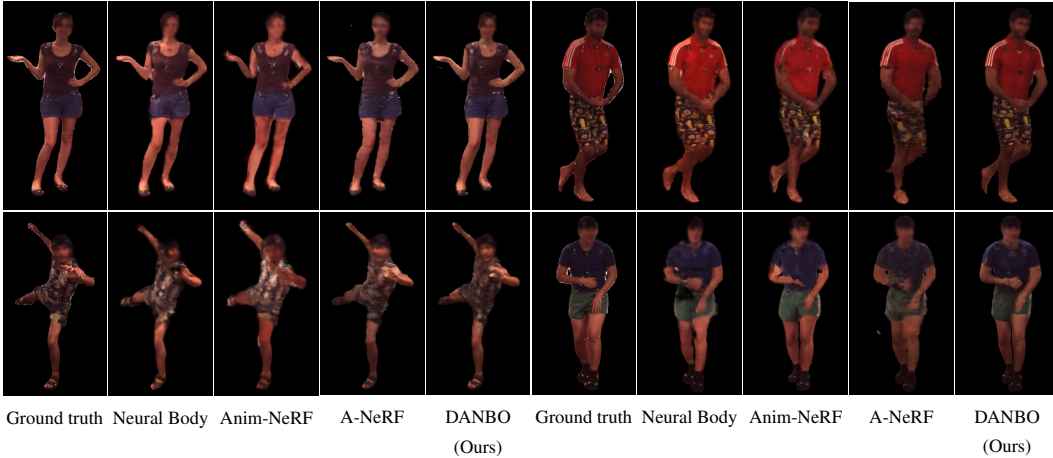


Figure 6: **Unseen pose synthesis on Human3.6M Ionescu et al. [2014] test split.** Our disentangled representation enables DANBO to generate plausible geometry and deformation for held-out testing poses, and achieve better visual quality than both surface-free and surface-based baselines. Note that, unlike Anim-NeRF Peng et al. [2021a], we do not require test-time finetuning for unseen poses.

Datasets. We compare our DANBO using the established benchmarks for neural bodies, covering indoor and outdoor, and single and multi-view settings:

- **Human3.6M**¹ Ionescu et al. [2011, 2014]: We follow the same evaluation protocol as in Anim-NeRF Peng et al. [2021a], with a total of 7 subjects for evaluation. The foreground maps are computed using Gong et al. [2018].
- **MonoPerfCap** Xu et al. [2018] features multiple outdoor sequences, recorded using a single high-resolution camera. We use the same two sequences and setting as in A-NeRF Su et al. [2021]: Weipeng_outdoor and Nadia_outdoor with 1151 and 1635 images, respectively, of resolution 1080×1920 . Human and camera pose is estimated by SPIN Kolotouros et al. [2019] and refined with Su et al. [2021]. Foreground masks are obtained by DeepLabv3 Chen et al. [2017].
- **Mixamo** Adobe [2020] is a synthetic dataset that includes challenging dancing motions. We use the sequences processed by Su et al. [2021] for motion retargeting.
- **Surreal** Varol et al. [2017] is a synthetic dataset animated using real-life motion capture data CMU-Mocap CMU Graphics Lab Motion Capture Database. It consists of diverse motion sequences such as gymnastic poses and ballet dances, making it a suitable dataset for testing out-of-distribution novel pose synthesis.

In total, we evaluate on 9 different subjects and 11 different sequences.

4.1 Novel View Synthesis

View synthesis of poses seen during training is simpler as the interplay between body parts is observable. Hence, our explicit disentanglement of body parts is less crucial but still beneficial. Compared

¹Meta did not have access to the Human3.6M dataset.



Figure 7: **Motion retargeting on Mixamo Adobe [2020] and CMU-Mocap CMU Graphics Lab Motion Capture Database dataset** with body models trained on various subjects. DANBO shows better robustness and generalization than the surface-free approach A-NeRF.

to the baselines, higher detail is present and body shape is better preserved, such as visible at facial features and arm contours in Figure 5. Anim-NeRF shows slightly distorted arms and cloud-like artifacts, potentially caused by incorrectly estimated deformation fields. Table 1 verifies these improvements in terms of PSNR and SSIM on the test set of Anim-NeRF Peng et al. [2021a].

4.2 Unseen Pose Synthesis and Animation

Rendering of unseen poses tests how well the learned pose-dependent deformations generalize. Figure 6 shows how differences are most prominent on limbs and faces. DANBO achieves better rendering quality and retains more consistent geometric details, generalizing well to both held out poses and out-of-distribution poses (see Figure 7). In Table 2, we report the PSNR and SSIM on the held-out testing sets. We attribute this to the improved localization via graph neural networks as well as the Soft-softmax that outperforms the default soft-max baseline, e.g., as used in Deng et al. [2019], Noguchi et al. [2021]. The ablation study below provides further insights.

Manual animation and driving of virtual models, e.g., in VR, requires such pose synthesis, for which Figure 7 provides animation examples. Note that no quantitative evaluation is possible here as no

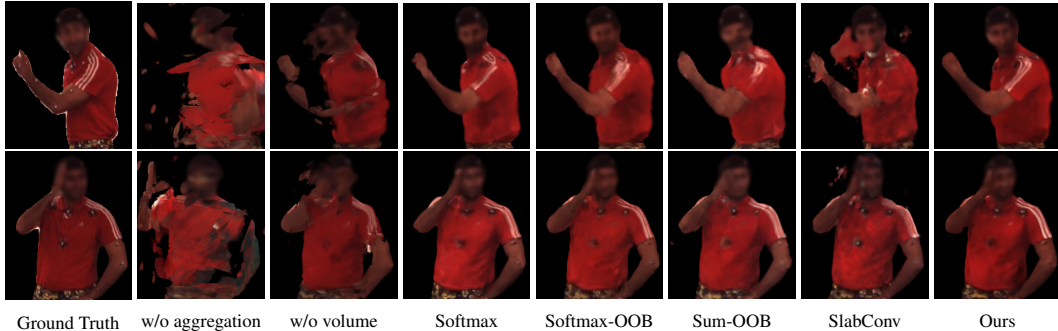


Figure 8: **Ablation study on Human3.6M Ionescu et al. [2014] test split novel pose (top row) and novel view (bottom row).** Our proposed designs together achieve better results with less distortion on the body parts, particularly in the limbs and face.

Table 2: **Novel-pose synthesis comparisons on Human3.6M Ionescu et al. [2014].** Our part-disentangled design enables DANBO to generalize better to unseen poses.

	NHRWu et al. [2020]		NT Thies et al. [2019]		NeuralBody Peng et al. [2021b]		Anim-NeRF Peng et al. [2021a]		A-NeRF Su et al. [2021]		DANBO (Ours)	
	PSNR \uparrow	SSIM \uparrow	PSNR \uparrow	SSIM \uparrow	PSNR \uparrow	SSIM \uparrow	PSNR \uparrow	SSIM \uparrow	PSNR \uparrow	SSIM \uparrow	PSNR \uparrow	SSIM \uparrow
S1	21.24	0.877	21.08	0.874	22.10	0.878	21.37	0.868	22.67	0.883	23.03	0.895
S5	21.55	0.883	21.06	0.879	23.52	0.897	22.29	0.875	22.96	0.888	23.66	0.903
S6	21.14	0.876	21.20	0.875	23.42	0.892	22.59	0.884	22.77	0.869	24.57	0.906
S7	20.52	0.878	21.15	0.878	22.59	0.893	22.22	0.878	22.80	0.880	23.08	0.897
S8	19.55	0.876	17.67	0.862	20.94	0.876	21.78	0.882	21.95	0.886	22.60	0.904
S9	23.02	0.883	23.10	0.883	23.05	0.885	23.73	0.886	24.16	0.889	24.79	0.904
S11	22.94	0.890	22.72	0.889	23.72	0.884	23.92	0.889	23.40	0.880	24.57	0.901
Avg	21.42	0.880	21.14	0.877	22.76	0.886	22.56	0.880	22.96	0.882	23.76	0.902

ground truth reference image is available in this mode. Note also that the more difficult outdoor sequences are trained from a monocular video, a setting supported only by few existing approaches. The qualitative examples validate that DANBO achieves better rendering quality on most subjects, and the poses generated by DANBO are sharper, with more consistent body parts, and suffer from less floating artifacts.

4.3 Ablation Study

We conduct the ablation study on S9 of Human3.6M using the same splits as before. To speed up iteration cycles, we reduce the training iterations to 100k, and use every other pose in the training set from the default configuration. We furthermore decreased the factorized volume resolution to $M = 10$. Figure 8 shows results on both novel pose and novel view for all variants.

Proposed Modules. In Table 3, we report how each of our proposed modules contributes to the final performance.

For Ours w/o learned aggregation, we simply concatenate all the retrieved voxel features as inputs to the NeRF network, which is similar to A-NeRF but using GNN features. This leads to poor generalization, and the w/o aggregation model predicts many floating artifacts in empty space. For Ours w/o volume, the GNN predicts per-bone feature vector instead of factorized volumes. In this variant, the aggregation network takes as input \hat{x}_i to predict per-bone weights. The feature to neural field F is the aggregated GNN feature and local coordinates. While the w/o volume variant achieves comparable results, the model suffers from overfitting, and produces distorted results on joints. In sum, both our aggregation network and per-bone volume designs provide useful inductive biases for learning robust and expressive models.

Aggregation Strategy. In Table 4, we show the evaluation results with different aggregation methods in Section 3.2. Strategy with out-of-bound handling shows better robustness to unseen poses, with our Soft-softmax aggregation works better than Softmax-OOB, and the unweighted variant SUM-OOB being the worst.

Table 3: Ablation study on each of proposed modules.

	PSNR \uparrow	SSIM \uparrow
Ours w/o aggregation	17.08	0.627
Ours w/o volume	24.24	0.892
Ours w/o GNN	23.87	0.896
Ours full	24.38	0.899

Choice of Volume Representation. In Table 5, we show the results of using both our factorized volumes, and full 3D volume predicted using SlabConv Lombardi et al. [2021]. We observe that SlabConv, while capturing finer texture details as the model is more expressive, is more prone to noises in the empty space. We conclude that more views and pose data are required for using SlabConv as the volume representation.

4.4 Resource Consumption

We compare to A-NeRF with layer width 448 (2.3M parameters) to match ours in capacity (2.5M) for a fair comparison. Using the factorized volume has a much lower parameter count than the conventional 3D grid (4.9M). Anim-NeRF smaller capacity (1.3M) and optimize a 128-dim latent vector for each pose to predict the deformation fields, and NeuralBody has the largest model capacity (5.0M). On the Nvidia V100 we used for training, DANBO takes on average 170 ms for every gradient descent iteration and around 6 seconds for synthesizing a 512×512 image. This is faster than A-NeRF with comparable capacity (around 8 seconds) but slower than Anim-NeRF (around 2 seconds).

5 Limitations and Discussion

Similar to other neural field-based approaches, the computation time for DANBO remains the limiting factor for real-time applications. While DANBO offers better generalization to unseen poses, we show in Figure 9 that in extreme cases it sometimes mixes the parts around joints together leading to deformation and blur. Handling such cases remains an open problem as also the surface-based method Anim-NeRF produces candy wrap artifacts around the elbow. It is also worth noting that DANBO is a person-specific model that needs to be trained individually for each person, which is desirable so long as sufficient training time and data is available.

6 Conclusion

We presented a surface-free approach for learning an animatable human body model from video. This is practical as it applies to monocular recordings, alleviates the restrictions of template or parametric models, and works in indoor and outdoor conditions. Our contributions on encoding pose locally with a GNN, factorized volumes, and a soft aggregation function improve upon existing models in the same class and even rival recent surface-based solutions.

References

- Adobe. Mixamo. <https://www.mixamo.com/>, 2020.
- T. Alldieck, H. Xu, and C. Sminchisescu. imghum: Implicit generative models of 3d human shape and articulated pose. In *ICCV*, 2021.
- T. Bagautdinov, C. Wu, T. Simon, F. Prada, T. Shiratori, S.-E. Wei, W. Xu, Y. Sheikh, and J. Saragih. Driving-signal aware full-body avatars. *ACM TOG (Proc. SIGGRAPH)*, 2021.
- A. O. Balan, L. Sigal, M. J. Black, J. E. Davis, and H. W. Haussecker. Detailed human shape and pose from images. In *CVPR*, pages 1–8, 2007.
- J. T. Barron, B. Mildenhall, M. Tancik, P. Hedman, R. Martin-Brualla, and P. P. Srinivasan. Mip-nerf: A multiscale representation for anti-aliasing neural radiance fields. *ICCV*, 2021.

Table 4: Ablation study of different aggregation methods.

	PSNR \uparrow	SSIM \uparrow
Softmax	23.80	0.896
Softmax-OOB	24.00	0.897
Sum-OOB	23.22	0.890
Sigmoid-OOB	23.75	0.896
Soft-softmax	24.38	0.899

Table 5: Ablation study of different type of coarse volumes.

	PSNR \uparrow	SSIM \uparrow
3D Volume (SlabConv) Lombardi et al. [2021]	24.17	0.892
Factorized Volume (Ours)	24.38	0.899

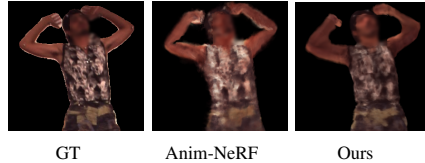


Figure 9: Unseen local poses create artifacts around the joints.

- B. L. Bhatnagar, C. Sminchisescu, C. Theobalt, and G. Pons-Moll. Combining implicit function learning and parametric models for 3d human reconstruction. In *ECCV*, 2020.
- A. Burov, M. Nießner, and J. Thies. Dynamic surface function networks for clothed human bodies. In *ICCV*, 2021.
- L.-C. Chen, G. Papandreou, F. Schroff, and H. Adam. Rethinking atrous convolution for semantic image segmentation. *arXiv preprint arXiv:1706.05587*, 2017.
- X. Chen, Y. Zheng, M. J. Black, O. Hilliges, and A. Geiger. Snarf: Differentiable forward skinning for animating non-rigid neural implicit shapes. In *ICCV*, 2021.
- V. Choutas, G. Pavlakos, T. Bolkart, D. Tzionas, and M. J. Black. Monocular expressive body regression through body-driven attention. In *ECCV*, 2020. URL <https://expose.is.tue.mpg.de>.
- CMU Graphics Lab Motion Capture Database. CMU Graphics Lab Motion Capture Database. <http://mocap.cs.cmu.edu>.
- E. Corona, A. Pumarola, G. Alenyà, G. Pons-Moll, and F. Moreno-Noguer. Smplicit: Topology-aware generative model for clothed people. In *CVPR*, 2021.
- B. Deng, J. Lewis, T. Jeruzalski, G. Pons-Moll, G. Hinton, M. Norouzi, and A. Tagliasacchi. Nasa: neural articulated shape approximation. *arXiv preprint arXiv:1912.03207*, 2019.
- G. Gafni, J. Thies, M. Zollhöfer, and M. Nießner. Dynamic neural radiance fields for monocular 4d facial avatar reconstruction. In *CVPR*, 2021.
- C. Gao, A. Saraf, J. Kopf, and J.-B. Huang. Dynamic view synthesis from dynamic monocular video. In *ICCV*, 2021.
- K. Gong, X. Liang, Y. Li, Y. Chen, M. Yang, and L. Lin. Instance-level human parsing via part grouping network. In *ECCV*, 2018.
- K. Guo, P. Lincoln, P. Davidson, J. Busch, X. Yu, M. Whalen, G. Harvey, S. Orts-Escolano, R. Pandey, J. Dourgarian, et al. The relightables: Volumetric performance capture of humans with realistic relighting. *ACM TOG (Proc. SIGGRAPH)*, 2019.
- M. Habermann, L. Liu, W. Xu, M. Zollhoefer, G. Pons-Moll, and C. Theobalt. Real-time deep dynamic characters. *ACM TOG (Proc. SIGGRAPH)*, 2021.
- C. Ionescu, F. Li, and C. Sminchisescu. Latent Structured Models for Human Pose Estimation. In *ICCV*, 2011.
- C. Ionescu, J. Carreira, and C. Sminchisescu. Iterated Second-Order Label Sensitive Pooling for 3D Human Pose Estimation. In *CVPR*, 2014.
- T. N. Kipf and M. Welling. Semi-supervised classification with graph convolutional networks. In *ICLR*, 2017.
- M. Kocabas, N. Athanasiou, and M. J. Black. Vibe: Video inference for human body pose and shape estimation. In *CVPR*, 2020.
- N. Kolotouros, G. Pavlakos, M. J. Black, and K. Daniilidis. Learning to reconstruct 3d human pose and shape via model-fitting in the loop. In *ICCV*, 2019.
- Y. Kwon, D. Kim, D. Ceylan, and H. Fuchs. Neural human performer: Learning generalizable radiance fields for human performance rendering. *NeurIPS*, 2021.
- C.-H. Lin, W.-C. Ma, A. Torralba, and S. Lucey. Barf: Bundle-adjusting neural radiance fields. *arXiv preprint arXiv:2104.06405*, 2021.
- D. B. Lindell, J. N. Martel, and G. Wetzstein. Autoint: Automatic integration for fast neural volume rendering. In *CVPR*, 2021.

- L. Liu, M. Habermann, V. Rudnev, K. Sarkar, J. Gu, and C. Theobalt. Neural actor: Neural free-view synthesis of human actors with pose control. *ACM TOG (Proc. SIGGRAPH Asia)*, 2021.
- S. Lombardi, T. Simon, G. Schwartz, M. Zollhoefer, Y. Sheikh, and J. Saragih. Mixture of volumetric primitives for efficient neural rendering. *ACM TOG (Proc. SIGGRAPH)*, 2021.
- M. Loper, N. Mahmood, J. Romero, G. Pons-Moll, and M. J. Black. Smpl: A skinned multi-person linear model. *ACM TOG (Proc. SIGGRAPH)*, 34(6):1–16, 2015.
- R. Martin-Brualla, N. Radwan, M. S. M. Sajjadi, J. T. Barron, A. Dosovitskiy, and D. Duckworth. NeRF in the Wild: Neural Radiance Fields for Unconstrained Photo Collections. In *CVPR*, 2021.
- B. Mildenhall, P. P. Srinivasan, M. Tancik, J. T. Barron, R. Ramamoorthi, and R. Ng. Nerf: Representing scenes as neural radiance fields for view synthesis. In *ECCV*, 2020.
- A. Noguchi, X. Sun, S. Lin, and T. Harada. Neural articulated radiance field. In *ICCV*, 2021.
- A. A. A. Osman, T. Bolkart, and M. J. Black. STAR: A sparse trained articulated human body regressor. In *ECCV*, 2020.
- J. J. Park, P. Florence, J. Straub, R. Newcombe, and S. Lovegrove. Deepsdf: Learning continuous signed distance functions for shape representation. In *CVPR*, 2019.
- K. Park, U. Sinha, P. Hedman, J. T. Barron, S. Bouaziz, D. B. Goldman, R. Martin-Brualla, and S. M. Seitz. Hypernerf: A higher-dimensional representation for topologically varying neural radiance fields. *ACM TOG (Proc. SIGGRAPH)*, 2021.
- S. Peng, M. Niemeyer, L. Mescheder, M. Pollefeys, and A. Geiger. Convolutional occupancy networks. In *ECCV*. Springer, 2020.
- S. Peng, J. Dong, Q. Wang, S. Zhang, Q. Shuai, X. Zhou, and H. Bao. Animatable neural radiance fields for modeling dynamic human bodies. In *ICCV*, 2021a.
- S. Peng, Y. Zhang, Y. Xu, Q. Wang, Q. Shuai, H. Bao, and X. Zhou. Neural body: Implicit neural representations with structured latent codes for novel view synthesis of dynamic humans. In *CVPR*, 2021b.
- A. Pumarola, E. Corona, G. Pons-Moll, and F. Moreno-Noguer. D-NeRF: Neural Radiance Fields for Dynamic Scenes. In *CVPR*, 2020.
- S. Saito, J. Yang, Q. Ma, and M. J. Black. SCANimate: Weakly supervised learning of skinned clothed avatar networks. In *CVPR*, 2021.
- V. Sitzmann, J. Martel, A. Bergman, D. Lindell, and G. Wetzstein. Implicit neural representations with periodic activation functions. *NeurIPS*, 33, 2020.
- S.-Y. Su, F. Yu, M. Zollhöfer, and H. Rhodin. A-nerf: Articulated neural radiance fields for learning human shape, appearance, and pose. In *NeurIPS*, 2021.
- J. Thies, M. Zollhöfer, and M. Nießner. Deferred neural rendering: Image synthesis using neural textures. *ACM TOG (Proc. SIGGRAPH)*, 2019.
- G. Tiwari, B. L. Bhatnagar, T. Tung, and G. Pons-Moll. Sizer: A dataset and model for parsing 3d clothing and learning size sensitive 3d clothing. In *ECCV*, 2020.
- G. Tiwari, N. Sarafianos, T. Tung, and G. Pons-Moll. Neural-gif: Neural generalized implicit functions for animating people in clothing. In *ICCV*, 2021.
- E. Tretschk, A. Tewari, V. Golyanik, M. Zollhöfer, C. Lassner, and C. Theobalt. Non-rigid neural radiance fields: Reconstruction and novel view synthesis of a dynamic scene from monocular video. In *ICCV*, 2021.
- G. Varol, J. Romero, X. Martin, N. Mahmood, M. J. Black, I. Laptev, and C. Schmid. Learning from synthetic humans. In *CVPR*, 2017.

- S. Wang, M. Mihajlovic, Q. Ma, A. Geiger, and S. Tang. Metaavatar: Learning animatable clothed human models from few depth images. In *NeurIPS*, 2021.
- Z. Wang, A. C. Bovik, H. R. Sheikh, and E. P. Simoncelli. Image quality assessment: from error visibility to structural similarity. *TIP*, 2004.
- M. Wu, Y. Wang, Q. Hu, and J. Yu. Multi-view neural human rendering. In *CVPR*, 2020.
- W. Xian, J.-B. Huang, J. Kopf, and C. Kim. Space-time neural irradiance fields for free-viewpoint video. In *CVPR*, 2021.
- H. Xu, E. G. Bazavan, A. Zanfir, W. T. Freeman, R. Sukthankar, and C. Sminchisescu. Ghum & ghuml: Generative 3d human shape and articulated pose models. In *CVPR*, 2020.
- H. Xu, T. Alldieck, and C. Sminchisescu. H-nerf: Neural radiance fields for rendering and temporal reconstruction of humans in motion. *NeurIPS*, 2021.
- W. Xu, A. Chatterjee, M. Zollhöfer, H. Rhodin, D. Mehta, H.-P. Seidel, and C. Theobalt. Monoperfcap: Human performance capture from monocular video. *TOG*, 37(2):27, 2018.
- L. Yen-Chen, P. Florence, J. T. Barron, A. Rodriguez, P. Isola, and T.-Y. Lin. inerf: Inverting neural radiance fields for pose estimation. In *IROS*, 2020.
- A. Yu, R. Li, M. Tancik, H. Li, R. Ng, and A. Kanazawa. PlenOctrees for real-time rendering of neural radiance fields. In *ICCV*, 2021a.
- A. Yu, V. Ye, M. Tancik, and A. Kanazawa. pixelNeRF: Neural radiance fields from one or few images. In *CVPR*, 2021b.
- X. Zhou, M. Zhu, G. Pavlakos, S. Leonardos, K. G. Derpanis, and K. Daniilidis. Monocap: Monocular human motion capture using a cnn coupled with a geometric prior. *PAMI*, 2018.
- Y. Zhou, C. Barnes, J. Lu, J. Yang, and H. Li. On the continuity of rotation representations in neural networks. In *CVPR*, pages 5745–5753, 2019.